

Exchange Bias and Quantum Anomalous Hall Effect in the $\text{MnBi}_2\text{Te}_4\text{-CrI}_3$ Heterostructure

Huixia Fu,¹ Chao-Xing Liu,^{2,*} and Binghai Yan^{1,†}

¹*Department of Condensed Matter Physics, Weizmann Institute of Science, Rehovot 7610001, Israel*

²*Department of Physics, the Pennsylvania State University, University Park, PA, 16802*

The layered antiferromagnetic MnBi_2Te_4 films have been proposed to be an intrinsic quantum anomalous Hall (QAH) insulator with a large gap. To realize this proposal, it is crucial to open a magnetic gap of surface states. However, recent experiments have observed gapless surface states [1–4], indicating the absence of out-of-plane surface magnetism, and thus the quantized Hall resistance can only be achieved at the magnetic field above 6 T [5–7]. In this work, we propose to induce out-of-plane surface magnetism of MnBi_2Te_4 films via the magnetic proximity with magnetic insulator CrI_3 . Our calculations have revealed a strong exchange bias ~ 40 meV, originating from the long $\text{Cr-}e_g$ orbital tails that hybridize strongly with Te p -orbitals. By stabilizing surface magnetism, the QAH effect can be realized in the $\text{MnBi}_2\text{Te}_4/\text{CrI}_3$ heterostructure. Our calculations also demonstrate the high Chern number QAH state can be achieved by controlling external electric gates. Thus, the $\text{MnBi}_2\text{Te}_4/\text{CrI}_3$ heterostructure provides a promising platform to realize the electrically tunable zero-field QAH effect.

Introduction: The quantum anomalous Hall (QAH) effect is a topological phenomenon characterized by quantized Hall resistance and zero longitudinal resistance [8–11]. Different from the conventional quantum Hall effect, the QAH effect is induced by the interplay between spin-orbit coupling (SOC) and magnetic exchange coupling, and thus can occur in certain ferromagnetic (FM) materials at zero external magnetic field. Owing to its topological and dissipation-free properties, the QAH insulator is an outstanding quantum-coherent material platform for the next-generation quantum-based technologies, including spintronics [12–14] and topological quantum computations [15]. Following the early theoretical predictions [16–18], the QAH effect was first demonstrated in magnetically (Cr or V) doped $(\text{Bi,Sb})_2\text{Te}_3$ [19–22], in which magnetic doping provides the required exchange coupling between magnetic moments and electron spins, and thus is essential for the occurrence of the QAH state. However, magnetic doping inevitably degrades sample quality with the presence of massive disorders and thus limits the critical temperature of the QAH state below 2K [22]. Therefore, it is desirable to realize the QAH effect in intrinsic magnetic materials with stoichiometric crystals.

Recently, a tetradymite-type layered compound, MnBi_2Te_4 , was proposed to be a promising topological material platform [23–26] with intrinsic A-type anti-ferromagnetic (AFM) order, in which the magnetic moments of Mn atoms are ferromagnetically coupled within one septuple layer (SL) and anti-ferromagnetically coupled between the adjacent SLs, for the realization of the QAH effect, as well as other magnetic topological phases [27–29]. Early first principles calculations show that the QAH state can be realized in the MnBi_2Te_4

films with odd number of SLs at zero magnetic field for the ideal AFM order [24, 25, 30]. The A-type AFM order was demonstrated via magnetization measurements for bulk MnBi_2Te_4 as the typical spin-flop transition was observed when the external magnetic field perpendicular to the SL plane was increased above 3.5T [5, 26, 31–34]. However, the magneto-transport experiments in the MnBi_2Te_4 films only revealed a quantized Hall resistance for the magnetic field above 6T [5–7], larger than the critical field of spin-flop transition. Therefore, the thin film has already become ferromagnetic under this magnetic field. The predicted zero-field QAH state induced by the ideal AFM order has yet been demonstrated experimentally. The early angular-resolved photon emission spectroscopy (ARPES) measurements observed a band gap, ranging from 50 meV to hundreds of meVs [26, 31, 35, 36], of topological surface states (TSSs) in MnBi_2Te_4 . However, this gap is shown to persist well above the Néel temperature and could be observed even at room temperature [26, 31, 35], making it unlikely originated from the AFM order. Indeed, more recent high-resolution ARPES studies based on synchrotron and laser light sources show that the TSS remains gapless below the Néel temperature [1–4]. The negligible magnetic gap of TSS is consistent with the absence of the zero-field QAH effect in magneto-transport measurements [5–7, 31, 33]. The absence of magnetic gap of TSSs suggests that the surface magnetism may not be well developed and different from the bulk AFM order. Physically, this is not surprising since more complex magnetic interactions, including dipole-dipole interaction and Dzyaloshinskii-Moriya interaction, may play an important role for the surface magnetic mechanism. Consequently, the surface Mn magnetic moments may be canted, or lie in the SL plane, or become disordered, all of which may lead to a gapless TSS. Furthermore, magnetic domains ubiquitously exist in AFM materials and cannot be easily eliminated even by field cooling. All these problems hamper the realization of zero-field QAH state in the MnBi_2Te_4 films.

* cxl56@psu.edu

† binghai.yan@weizmann.ac.il

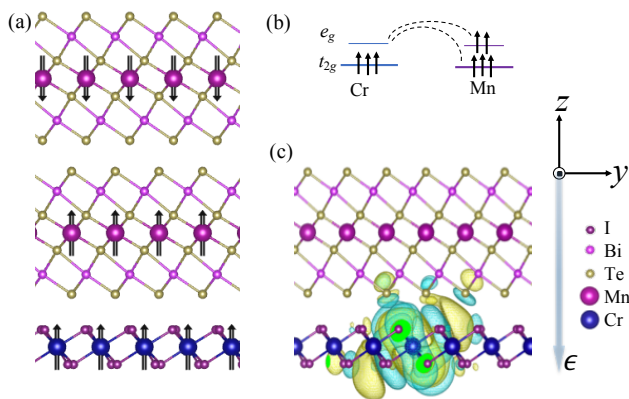


FIG. 1. The atomic structure of the MnBi₂Te₄/CrI₃ heterostructure. (a) MnBi₂Te₄ and CrI₃ prefers the ferromagnetic type coupling while MnBi₂Te₄ layers remains the antiferromagnetic interaction. (b) Schematics of the exchange interaction between Cr-*e_g* and Mn-*e_gt_{2g}* states. (c) The Wannier function of one of Cr-*e_g* states. Its tails reach the neighboring Te atoms by crossing the van der Waals gap. Yellow and cyan colors represent positive and negative, respectively, isovalue surfaces of the Wannier function. An external electric field (ϵ) along $-z$ can lift the energy of Cr-*e_g* bands.

In this work, we propose to overcome the challenge of surface magnetism by coupling the MnBi₂Te₄ films to a two-dimensional (2D) ferromagnetic insulator with the example of CrI₃ via exchange bias. Our density-functional theory (DFT) calculations on the MnBi₂Te₄/CrI₃ heterostructure show a ferromagnetic exchange bias around 40 meV, much larger than the Néel temperature of MnBi₂Te₄ (24 K [26]) and the Curie temperature of CrI₃ (61 K for bulk [37] and 45 K for monolayer[38]). Moreover, CrI₃ has little influence on electronic band structure of MnBi₂Te₄ films and thus the QAH state with the Chern number (CN) = 1 can exist in 3- and 5-SL-thick MnBi₂Te₄, consistent with the early studies on pure MnBi₂Te₄ films. We also studied the electric gating effect and the CrI₃/MnBi₂Te₄/CrI₃ heterostructures. Our results show (i) the high-CN QAH state with CN=3 can be achieved by tuning gate voltages and (ii) the strong exchange bias can always align the magnetization of both surfaces of MnBi₂Te₄ films, thus driving even SL MnBi₂Te₄ into the QAH state in the CrI₃/MnBi₂Te₄/CrI₃ heterostructure.

Ferromagnetic exchange bias at the MnBi₂Te₄/CrI₃ interface: The required exchange bias material should provide strong magnetic coupling at the interface but not change the electronic states near the Fermi energy. Therefore, we choose a magnetic insulator, CrI₃[38]. Its monolayer is ferromagnetic (FM) and can couple with MnBi₂Te₄ through the van der Waals interface, which may disturb the band structure of MnBi₂Te₄ weakly. Because the interaction is determined by the interface layer, we only choose a monolayer of CrI₃ for the interface model.

We construct interface models with one layer of CrI₃

and different layers of MnBi₂Te₄ on its top, as shown in Fig. 1. Both materials share the same triangular lattice but different in-plane lattice parameters, 7.04 Å for CrI₃ and 4.36 Å for MnBi₂Te₄ from our DFT calculations, which is consistent with recent works[24, 39, 40]. A 2×2 supercell of CrI₃ can match well with a 3×3 supercell of MnBi₂Te₄. Alternatively, the primitive unitcell of CrI₃ can also match a $\sqrt{3} \times \sqrt{3}$ supercell of MnBi₂Te₄ with a mismatch of 7%. Because we are mostly interested in the band structure of MnBi₂Te₄, we stretch the CrI₃ lattice to match the $\sqrt{3} \times \sqrt{3}$ MnBi₂Te₄ supercell. We fully optimized the atomic structures by including the van der Waals interactions in DFT calculations[41] within the generalized-gradient approximation (GGA)[42]. We have tested both models and found that they give similar results in the exchange coupling and band structure (see more information in the Supplementary Materials (SM) [43]). Thus, we choose the smaller model, $\sqrt{3} \times \sqrt{3}$ MnBi₂Te₄/1 \times 1 CrI₃, for further investigations in the following.

At the interface, MnBi₂Te₄ exhibits strong the FM coupling with CrI₃. For 1 SL MnBi₂Te₄ on top of CrI₃, the energy difference between the FM and AFM coupling is about 40 meV. We note that different ways of stacking between two materials give very similar strength of exchange coupling, which is also true for the 3×3 MnBi₂Te₄/2 \times 2 CrI₃ case [43]. When increasing the MnBi₂Te₄ layer to 2 SLs and more, the interface FM coupling remains with the same exchange energy and the two SLs couples still in the AFM way. Therefore, CrI₃ layer couples only with the neighboring MnBi₂Te₄ layer and does not affect the AFM order between different MnBi₂Te₄ layers. We point out that such an exchange coupling is much stronger than the magnitude of the exchange interactions between two MnBi₂Te₄ layers (~ 3 meV for $\sqrt{3} \times \sqrt{3}$ supercell) or two CrI₃ layers (~ 10 meV for 1 \times 1 unitcell[44]). Therefore, CrI₃ can stably pin the FM order of the proximity MnBi₂Te₄ layer and act as an effective exchange bias. In addition, we find that SOC does not affect the magnetic coupling at the interface.

The strong exchange coupling originates in the orbital feature at the interface. The Mn site has *d*⁵ configuration as *t*_{2g}³*e*_g² and the Cr site has *d*³ as *t*_{2g}³*e*_g⁰. There is a long exchange pathway from Cr-*e_g* to Mn-*t*_{2g} states through the intermediate I, Te, Bi and Te atoms, which is clearly beyond the simple super-exchange interaction. In the localized Wannier orbitals [45], we observe a crucial feature in the Cr-*e_g* states. Tails of the Cr-*e_g* Wannier functions extend beyond the van der Waals gap and strongly overlap with the neighboring Te-*p* orbitals (see Fig. 1c). This strong orbital overlap rationalizes the strong coupling between two materials. In addition, we note that AFM type coupling at the interface can also play a role of the exchange bias, although the present specific interface structure exhibits the FM coupling.

QAH effect: We next investigate the electronic band structure and discuss its topological properties. Figure 2 shows band structures for 1-6 MnBi₂Te₄ SL(s) on top of

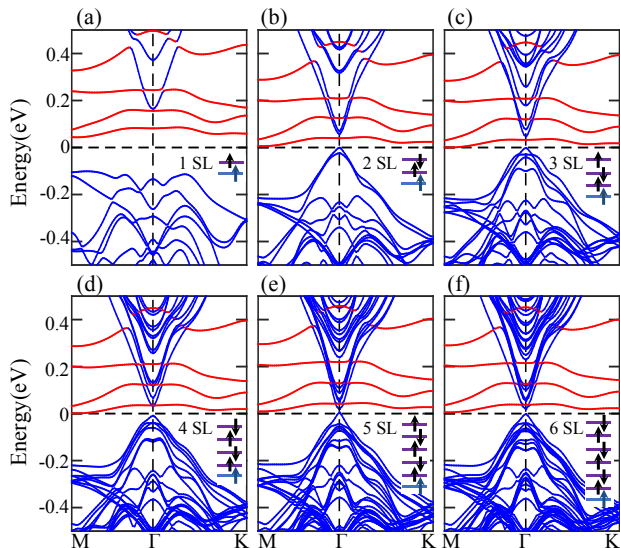


FIG. 2. Band structures of MnBi_2Te_4 thin films in proximity to a CrI_3 layer. From 1 to 6 - septuple layer (SL) - thick MnBi_2Te_4 are shown. Red lines indicate $\text{Cr-}e_g$ bands and blue ones for MnBi_2Te_4 bands. The Fermi energy is set to zero.

CrI_3 . As discussed above, there is FM coupling between CrI_3 and neighboring the MnBi_2Te_4 SL and AFM coupling between MnBi_2Te_4 SLs. The interface band structure can be approximately regarded as an overlap of two different materials. An essential feature is the existence of an energy gap in these band structures, which is crucial for the realization of QAH effect. The occupied $\text{Cr-}t_{2g}$ bands are far below the valence bands of MnBi_2Te_4 . The $\text{Cr-}e_g$ states overlap with the conduction band bottom of MnBi_2Te_4 and remain unoccupied. This means there is no charge transfer through the van der Waals junction. The calculated $\text{Cr-}t_{2g}$ and $\text{Cr-}e_g$ gap is about 1 eV, which is consistent with previous GGA calculations and can be corrected to about 1.5 eV by hybrid-functionals [46]. Although some $\text{Cr-}e_g$ bands appear as the lowest conduction bands at the interface for thinner MnBi_2Te_4 films (1-4 SLs), they do not affect our understanding of the band structure topology. When the MnBi_2Te_4 layer is thicker (e.g. 5-6 SLs), the MnBi_2Te_4 states become the lowest conduction bands. Thus, CrI_3 serves an ideal proximity exchange bias without destroying the MnBi_2Te_4 band structure.

We find that isolate MnBi_2Te_4 layers are trivial magnetic insulators for 1, 2, 4 and 6 SLs thick and QAHE insulators for 3 and 5 SLs, which is consistent with recent theoretical studies [24, 30]. Here, the QAH insulator possesses the $\text{CN} = 1$, as showed by our Berry phase calculations using the Wilson loop method [47, 48] in the 2D Brillouin zone. In proximity to the CrI_3 layer, MnBi_2Te_4 band structures are modified weakly without changing their topological nature. For example, the isolated MnBi_2Te_4 layer of 2, 4 or 6 SLs thick exhibits the

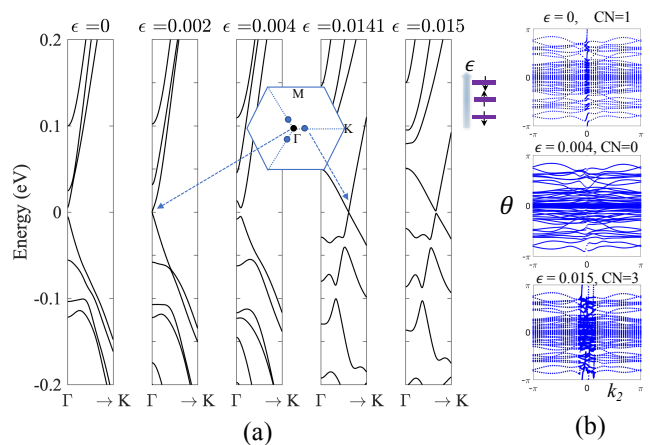


FIG. 3. (a) Band structure evolution of a 3-SL-thick as increasing the electric field (ϵ). Two topological transitions occur at $\epsilon = 0.002$ at the Γ point and 0.0141 V/Å along $\Gamma - K$ lines. (b) The Berry phase θ , i.e. the Wannier charge center, accumulated along a Wilson loop ($k_1 \in [-\pi, \pi]$) as varying k_2 . It is topologically equivalent to the edge state spectra. Corresponding Chern numbers (CN) are one, zero and three for $\epsilon = 0.00, 0.004$ and 0.015 V/Å, respectively.

double degeneracy in the band structure caused by the symmetry combining spatial inversion and time reversal. The existence of the CrI_3 layer breaks weakly this symmetry and splits the degenerate bands. We verify the topological character of the interface structures by observing the band gap evolution with respect to the SOC strength. For 3 and 5 SLs thick $\text{MnBi}_2\text{Te}_4 / \text{CrI}_3$, the band gap closes at about 90% of the normal SOC strength but re-opens an energy gap as increasing SOC, showing a topological phase transition (TPT)[43]. The QAH insulator gaps are 49 and 14 meV for the 3 and 5 SLs interface, respectively. For 1, 2, 4 and 6 SLs thick $\text{MnBi}_2\text{Te}_4 / \text{CrI}_3$, however, the band gap remains open as varying SOC from 0 to 100%. (see more information in Ref. [43]).

Electrically tunable high-Chern-number QAH effect: The 2D layered structure offers an opportunity to tune the band structure topology by applying a vertical electric field. The electric field induces different potential variation at different layers and subsequently modifies the overall band structure and its topological nature. For the interface structure, an electric field (ϵ) along the $-z$ direction can push the $\text{Cr-}e_g$ states up in the conduction band, as illustrated in Fig. 1b, leaving only MnBi_2Te_4 states right above and below the energy gap. Further increasing the electric field can induce an inversion between the occupied and unoccupied bands, giving rise to the TPT. Since the CrI_3 brings little modifications to the low-energy band structure of MnBi_2Te_4 , we only consider isolated MnBi_2Te_4 models when applying an electric field in following discussions.

The electric field can induce the high-CN QAH state. In a simple two-band model[16], a band inversion at the

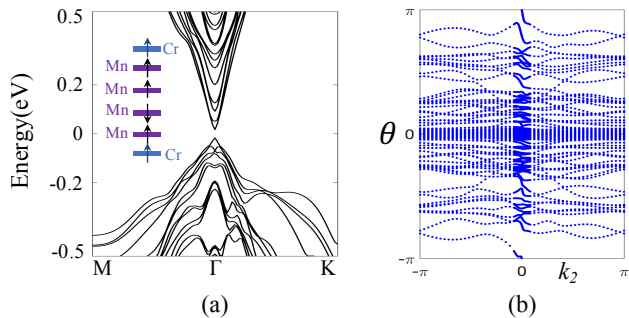


FIG. 4. (a) Band structure of a 4-SL-thick MnBi_2Te_4 with a special magnetic order. When it was sandwiched between two CrI_3 layers, the antiferromagnetic type coupling between MnBi_2Te_4 layers are changed by the top CrI_3 layer, as illustrated in the inset. (b) Corresponding Berry phase of the Wilson loop, with a Chern number $\text{CN} = -1$.

Γ point usually leads to a change of the CN by ± 1 . If the band inversion occurs at generic k-points, it can induce a jump of the CN by the number of the transition points. The MnBi_2Te_4 film under an electric field exhibits two important symmetries, the three-fold rotation (denoted as C_3) and a combined symmetry between the time-reversal and mirror reflection (denoted as TM). Since the mirror plane crosses the $\Gamma - M$ line in the Brillouin zone and perpendicular to the layer plane, the $\Gamma - K$ line is invariant under the TM symmetry. Therefore, if a transition happens at a generic k-point away from the $\Gamma - K$ line, the gapless points must exist at six different k-points related by the C_3 and TM symmetries. If a transition happens along the $\Gamma - K$ line that is invariant under TM , the gapless points must simultaneously appear at three different k-points related by C_3 (See the inset of Fig. 3a). If a transition appears at Γ that is invariant under both C_3 and TM symmetries, a single Dirac point transition can occur.

To verify this scenario, we carried out band structure calculations on 3-SL-thick MnBi_2Te_4 and demonstrate that the CN can jump by both 1 and 3 via applying a small electric field, as shown in Fig. 3. At zero electric field, the 3-SL-thick MnBi_2Te_4 is a QAH state with CN 1 and changes to a trivial insulator for $\epsilon = 0.005 \text{ V/\AA}$. This transition is through a gap-closing point at Γ for $\epsilon = 0.002/\text{\AA}$. For a larger electric field ($\epsilon = 0.015 \text{ V/\AA}$), another transition occurs with three gap-closing points along the $\Gamma - K$ lines, leading to a QAH state with $\text{CN} = 3$. Furthermore, the electric field can also drive the MnBi_2Te_4 film with even number of SLs from a trivial magnetic insulator with zero CN to the QAH state. For instance, $\epsilon = 0.03 \text{ V/\AA}$ induces a TPT with three gapless points along the $\Gamma - K$ lines in the 2-SL-thick MnBi_2Te_4 film at $\epsilon = 0.023 \text{ V/\AA}$, resulting in the QAH state with $\text{CN} = 3$ (See more information in SM [43]).

Sandwiched MnBi_2Te_4 structures: Given the short range nature of exchange bias, the CrI_3 is expected to

align the magnetization of the bottom MnBi_2Te_4 layer in the $\text{MnBi}_2\text{Te}_4/\text{CrI}_3$ heterostructure, but may have little influence on the top MnBi_2Te_4 layer when the film thickness is large. This issue can be resolved by considering a sandwiched structure $\text{CrI}_3/\text{MnBi}_2\text{Te}_4/\text{CrI}_3$. For the MnBi_2Te_4 films with an odd number of SLs, the AFM order in MnBi_2Te_4 is compatible with the FM orders in the top and bottom CrI_3 monolayers. In contrast, for the MnBi_2Te_4 films with an even number of SLs, the compensated AFM ordering between MnBi_2Te_4 layers can be changed by CrI_3 . As an example of the 4-SL case in Fig. 4, the magnetization of the top MnBi_2Te_4 SL feels frustration from the upper CrI_3 layer and the lower MnBi_2Te_4 layer. Because the $\text{MnBi}_2\text{Te}_4 - \text{CrI}_3$ coupling is much stronger than the $\text{MnBi}_2\text{Te}_4 - \text{MnBi}_2\text{Te}_4$ coupling, magnetic moments of the top MnBi_2Te_4 SL aligns parallel to those of the CrI_3 layer. Such a re-arrangement of magnetic moments in the MnBi_2Te_4 SL leads to a net magnetization for the MnBi_2Te_4 film. As verified by our band structure calculations, reversing magnetic moments of the top MnBi_2Te_4 SL layer is indeed energetically favored by $\sim 40 \text{ meV}$. Subsequently the system becomes a QAH state with an energy gap of 34 meV . As shown by the Wilson loop calculations, it exhibits a nontrivial $\text{CN} = -1$. Therefore, the sandwich configuration may always provide a QAH insulator for either odd or even number of MnBi_2Te_4 SLs.

Discussion and Conclusion: In summary, the magnetic order of MnBi_2Te_4 thin film can be pinned and also manipulated by a strong exchange bias in proximity to CrI_3 . Thus, the heterostructures with MnBi_2Te_4 and CrI_3 provide an experimentally feasible platform to realize the QAH effect. An external electric field can further modify the thin film band structure and induce QAH effect with large CNs. Since the magnetic insulator CrI_3 disturbs weakly the electronic states of MnBi_2Te_4 , it can also be used to pin the surface magnetic order of the bulk MnBi_2Te_4 and assist the observation of the axion insulator phase[27, 28] in ARPES. Additionally, it is worth noting that other magnetic insulators with out-of-plane magnetization, such as $\text{Tm}_3\text{Fe}_5\text{O}_{12}$ (TmIG)[49] and $\text{Cr}_2\text{Ge}_2\text{Te}_6$ [50], may also play the same role of exchange bias as CrI_3 .

Acknowledgement: We acknowledge helpful discussions with Cui-zu Chang and Xiaodong Xu. Work at Penn State (CXL) was primarily supported by the U.S. Department of Energy (DOE), Office of Science, Basic Energy Sciences (BES) under Award DE-SC0019064. CXL also acknowledges the support from the Office of Naval Research (Grant No. N00014-18-1-2793) and Kaufman New Initiative research grant KA2018-98553 of the Pittsburgh Foundation. B.Y. acknowledges the financial support by the Willner Family Leadership Institute for the Weizmann Institute of Science, the Benozio Endowment Fund for the Advancement of Science, Ruth and Herman Albert Scholars Program for New Scientists, the European Research Council (ERC) under the European Union's Horizon 2020 research and innovation pro-

-
- [1] Y.-J. Hao, P. Liu, Y. Feng, X.-M. Ma, E. F. Schwier, M. Arita, S. Kumar, C. Hu, R. Lu, M. Zeng, Y. Wang, Z. Hao, H. Sun, K. Zhang, J. Mei, N. Ni, L. Wu, K. Shimada, C. Chen, Q. Liu, and C. Liu, (2019), [1907.03722](#).
- [2] Y. J. Chen, L. X. Xu, J. H. Li, Y. W. Li, C. F. Zhang, H. Li, Y. Wu, A. J. Liang, C. Chen, S. W. Jung, C. Cacho, H. Y. Wang, Y. H. Mao, S. Liu, M. X. Wang, Y. F. Guo, Y. Xu, Z. K. Liu, L. X. Yang, and Y. L. Chen, (2019), [1907.05119](#).
- [3] H. Li, S.-Y. Gao, S.-F. Duan, Y.-F. Xu, K.-J. Zhu, S.-J. Tian, W.-H. Fan, Z.-C. Rao, J.-R. Huang, J.-J. Li, Z.-T. Liu, W.-L. Liu, Y.-B. Huang, Y.-L. Li, Y. Liu, G.-B. Zhang, H.-C. Lei, Y.-G. Shi, W.-T. Zhang, H.-M. Weng, T. Qian, and H. Ding, (2019), [1907.06491](#).
- [4] P. Swatek, Y. Wu, L.-L. Wang, K. Lee, B. Schruck, J. Yan, and A. Kaminski, (2019), [1907.09596](#).
- [5] Y. Deng, Y. Yu, M. Z. Shi, J. Wang, X. H. Chen, and Y. Zhang, (2019), [1904.11468](#).
- [6] C. Liu, Y. Wang, H. Li, Y. Wu, Y. Li, J. Li, K. He, Y. Xu, J. Zhang, and Y. Wang, (2019), [1905.00715](#).
- [7] J. Ge, Y. Liu, J. Li, H. Li, T. Luo, Y. Wu, Y. Xu, and J. Wang, (2019), [1907.09947](#).
- [8] F. D. M. Haldane, Phys. Rev. Lett. **61**, 2015 (1988).
- [9] C.-X. Liu, S.-C. Zhang, and X.-L. Qi, Annual Review of Condensed Matter Physics **7**, 301 (2016).
- [10] C.-Z. Chang and M. Li, Journal of Physics: Condensed Matter **28**, 123002 (2016).
- [11] J. Wang, B. Lian, and S.-C. Zhang, Physica Scripta **2015**, 014003 (2015).
- [12] I. Zutic, J. Fabian, and S. Das Sarma, Rev. Mod. Phys. **76**, 323 (2004).
- [13] J. E. Moore, Nature **464**, 194 (2010).
- [14] L. Šmejkal, Y. Mokrousov, B. Yan, and A. H. MacDonald, Nature Physics **14**, 242 (2018).
- [15] C. Nayak, S. H. Simon, A. Stern, M. Freedman, and S. Das Sarma, Rev. Mod. Phys. **80**, 1083 (2008).
- [16] X.-L. Qi, Y.-S. Wu, and S.-C. Zhang, Phys. Rev. B **74**, 085308 (2006).
- [17] C.-X. Liu, X.-L. Qi, X. Dai, Z. Fang, and S.-C. Zhang, Physical review letters **101** (2008).
- [18] R. Yu, W. Zhang, H. J. Zhang, S. C. Zhang, X. Dai, and Z. Fang, Science **329**, 61 (2010).
- [19] C. Chang, J. Zhang, X. Feng, J. Shen, Z. Zhang, M. Guo, K. Li, Y. Ou, P. Wei, L. Wang, Z. Q. Ji, Y. Feng, S. Ji, X. Chen, J. Jia, X. Dai, Z. Fang, S. C. Zhang, K. He, Y. Wang, L. Lu, X. C. Ma, and Q.-K. Xue, Science **340**, 167 (2013).
- [20] J. G. Checkelsky, R. Yoshimi, A. Tsukazaki, K. S. Takahashi, Y. Kozuka, J. Falson, M. Kawasaki, and Y. Tokura, Nature Physics **10**, 731 (2014).
- [21] X. Kou, S.-T. Guo, Y. Fan, L. Pan, M. Lang, Y. Jiang, Q. Shao, T. Nie, K. Murata, J. Tang, Y. Wang, L. He, T.-K. Lee, W.-L. Lee, and K. L. Wang, Phys. Rev. Lett. **113**, 137201 (2014).
- [22] C.-Z. Chang, W. Zhao, D. Y. Kim, H. Zhang, B. A. Assaf, D. Heiman, S.-C. Zhang, C. Liu, M. H. W. Chan, and J. S. Moodera, Nature Materials **14**, 473 (2015).
- [23] Y. Gong, J. Guo, J. Li, K. Zhu, M. Liao, X. Liu, Q. Zhang, L. Gu, L. Tang, X. Feng, D. Zhang, W. Li, C. Song, L. Wang, P. Yu, X. Chen, Y. Wang, H. Yao, W. Duan, Y. Xu, S.-C. Zhang, X. Ma, Q.-K. Xue, and K. He, Chinese Phys. Lett. **36**, 076801 (2019).
- [24] J. Li, Y. Li, S. Du, Z. Wang, B.-L. Gu, S.-C. Zhang, K. He, W. Duan, and Y. Xu, Science Advances **5**, eaaw5685 (2019).
- [25] D. Zhang, M. Shi, T. Zhu, D. Xing, H. Zhang, and J. Wang, Phys. Rev. Lett. **122**, 206401 (2019).
- [26] M. M. Otrokov, I. I. Klimovskikh, H. Bentmann, A. Zeugner, Z. S. Aliev, S. Gass, A. U. Wolter, A. V. Koroleva, D. Estyunin, A. M. Shikin, *et al.*, [arXiv:1809.07389](#) (2018).
- [27] X.-L. Qi, T. L. Hughes, and S.-C. Zhang, Phys. Rev. B **78**, 195424 (2008).
- [28] R. S. K. Mong, A. M. Essin, and J. E. Moore, Phys. Rev. B **81**, 245209 (2010).
- [29] X. Wan, A. M. Turner, A. Vishwanath, and S. Y. Savrasov, Phys. Rev. B **83**, 205101 (2011).
- [30] M. M. Otrokov, I. P. Rusinov, M. Blanco-Rey, M. Hoffmann, A. Y. Vyazovskaya, S. V. Eremeev, A. Ernst, P. M. Echenique, A. Arnau, and E. V. Chulkov, Phys. Rev. Lett. **122**, 107202 (2019).
- [31] S. H. Lee, Y. Zhu, Y. Wang, L. Miao, T. Pillsbury, S. Kempinger, D. Graf, N. Alem, C.-Z. Chang, N. Samarth, and Z. Mao, (2018), [1812.00339](#).
- [32] J. Q. Yan, S. Okamoto, M. A. McGuire, A. F. May, R. J. McQueeney, and B. C. Sales, (2019), [1905.00400](#).
- [33] J. Wu, F. Liu, M. Sasase, K. Ienaga, Y. Obata, R. Yukawa, K. Horiba, H. Kumigashira, S. Okuma, T. Inoshita, and H. Hosono, (2019), [1905.02385](#).
- [34] K. Y. Chen, B. S. Wang, J. Q. Yan, D. S. Parker, J. S. Zhou, Y. Uwatoko, and J. G. Cheng, (2019), [1907.01760](#).
- [35] R. Vidal, H. Bentmann, T. Peixoto, A. Zeugner, S. Moser, C. Min, S. Schatz, K. Kissner, M. Ünzelmann, C. Fornari, *et al.*, arXiv preprint arXiv:1903.11826 (2019).
- [36] B. Chen, F. Fei, D. Zhang, B. Zhang, W. Liu, S. Zhang, P. Wang, B. Wei, Y. Zhang, J. Guo, *et al.*, arXiv preprint arXiv:1903.09934 (2019).
- [37] M. A. McGuire, H. Dixit, V. R. Cooper, and B. C. Sales, Chem. Mater. **27**, 612 (2015).
- [38] B. Huang, G. Clark, E. Navarro-Moratalla, D. R. Klein, R. Cheng, K. L. Seyler, D. Zhong, E. Schmidgall, M. A. McGuire, D. H. Cobden, W. Yao, D. Xiao, P. Jarillo-Herrero, and X. Xu, Nature **546**, 270 (2017).
- [39] Y. Hou, J. Kim, and R. Wu, Science Advances **5**, eaaw1874 (2019).
- [40] D. Zhang, M. Shi, K. He, D. Xing, H. Zhang, and J. Wang, [arXiv:1808.08014](#) (2018).
- [41] G. Kresse and J. Furthmüller, Phys. Rev. B **54**, 11169 (1996).
- [42] J. P. Perdew, K. Burke, and M. Ernzerhof, Phys. Rev. Lett. **77**, 3865 (1996).
- [43] *More information can be found in the Appendice (Supplementary Materials).*
- [44] N. Sivadas, S. Okamoto, X. Xu, C. J. Fennie, and D. Xiao, Nano Lett. **18**, 7658 (2018).

- [45] A. A. Mostofi, J. R. Yates, Y.-S. Lee, I. Souza, D. Vanderbilt, and N. Marzari, *Comput. Phys. Commun.* **178**, 685 (2008).
- [46] W.-B. Zhang, Q. Qu, P. Zhu, and C.-H. Lam, *Journal of Materials Chemistry C* **3**, 12457 (2015).
- [47] R. Yu, X.-L. Qi, A. Bernevig, Z. Fang, and X. Dai, *Phys. Rev. B* **84**, 075119 (2011).
- [48] A. A. Soluyanov and D. Vanderbilt, *Phys. Rev. B* **83**, 035108 (2011).
- [49] C. O. Avci, A. Quindeau, C.-F. Pai, M. Mann, L. Caretta, A. S. Tang, M. C. Onbasli, C. A. Ross, and G. S. D. Beach, *Nature Materials* **16**, 309 (2017).
- [50] C. Gong, L. Li, Z. Li, H. Ji, A. Stern, Y. Xia, T. Cao, W. Bao, C. Wang, Y. Wang, Z. Q. Qiu, R. J. Cava, S. G. Louie, J. Xia, and X. Zhang, *Nature* **546**, 265 (2017).

Appendix 1: Calculation Methods

Density functional theory (DFT) calculations were performed using the Vienna ab initio simulation package (VASP) with core electrons represented by the projector-augmented-wave (PAW) potential. Plane waves with a kinetic energy cutoff of 270 eV were used as the basis set. Geometry optimization was carried out until the residual force on each atom was less than 0.01 eV/Å. We projected the Wannier functions of the bulk MnBi_2Te_4 in the AFM phase. Based on the bulk tight-binding parameters of Wannier functions, we constructed the slab model for MnBi_2Te_4 thin films and evaluated their band structures and Berry phases.



	Stacking type A (C_3)		Stacking type B (C_1)	
	ΔE (w/o SOC)	ΔE (SOC)	ΔE (w/o SOC)	ΔE (SOC)
$\Delta E = E_{\text{FM}} - E_{\text{AFM}}$ (meV)	-42	-38	-42	-42

FIG. S1. The magnetic coupling energy ΔE for different stacking way of the interface for 1-SL MnBi_2Te_4 on CrI_3 . The type-A stacking has C_3 rotational symmetry while the type-B has no. Results with and without spin-orbit coupling (SOC) are shown. Different way of stacking and SOC as well do not sensitively modify the exchange coupling at the interface.

TABLE S1. The gap at Γ from MnBi_2Te_4 bands of the heterostructures. When placing MnBi_2Te_4 on top of CrI_3 , the whole system remains to be insulating. Here, we show the band gap of the MnBi_2Te_4 thin film as shown in Fig. 2.

Thickness (SL)	1	2	3	4	5	6
Gap (meV)	299	59	49	42	14	22

Appendix 2: Structure models and exchange coupling

In the interface model, we can overlap the CrI_3 layer and the MnBi_2Te_4 layer with different sliding shift in the plane. We have tested different ways of stacking and found they give quantitatively very similar results in energy and band structure for the $\sqrt{3} \times \sqrt{3}$ $\text{MnBi}_2\text{Te}_4/1 \times 1$ CrI_3 interface. At the same FM phase,

the stacking way that preserves the three-fold rotation (C_3) exhibits slightly lower energy (by 20~30 meV for 1 to 3 MnBi_2Te_4 SLs) than other low-symmetry stacking ways. Therefore, we used the C_3 -symmetric model in the main text.

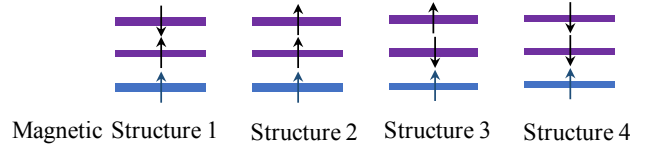
We show the exchange coupling $\Delta E = E_{\text{FM}} - E_{\text{AFM}}$ for 1-2 SL MnBi_2Te_4 on a CrI_3 layer in Figs.S1 and S2. Two different stacking ways give similar exchange coupling strength. One can also deduce that the MnBi_2Te_4 - MnBi_2Te_4 interlayer coupling (~ 4 meV) is much weaker than the MnBi_2Te_4 - CrI_3 coupling (~ 40 meV) from Fig.S2.

For the much larger supercell, 3×3 $\text{MnBi}_2\text{Te}_4/2 \times 2$ CrI_3 , it still prefers the FM coupling at the interface with an exchange coupling energy ~ 40 meV. The system remains as an insulator, as shown in Fig. S3.

The band gaps for different SLs of MnBi_2Te_4 films (Fig.2) are shown in the table S1.

Figure S4 show the energies of different magnetic configurations of 4-SL of MnBi_2Te_4 sandwiched between two CrI_3 layers. The structure 1, in which the top MnBi_2Te_4 SL flips its spin direction due to the top CrI_3 layer, has the lowest energy. In the band structure, $\text{Cr}-e_g$ states appear as the conduction bands. There is still an energy gap for the QAH state with $\text{CN} = -1$, as shown in Fig. 4.

Figures S5 and S6 show the band evolution as increasing SOC strength for 3 and 5 SL MnBi_2Te_4 , respectively. The band gap closing is found when the SOC strength is increased to 90% (98%) of the full SOC strength for 3 (5) SL MnBi_2Te_4 , reflecting the occurrence of TPT and the change of CN.



Magnetic structure	Stacking type A (C_3)	Stacking type B (C_1)
	ΔE (w/o SOC)	ΔE (w/o SOC)
1	0	0
2	4	6
3	45	40
4	48	45

FIG. S2. The total energy ΔE for different magnetic structures of the interface for 2-SL MnBi_2Te_4 on CrI_3 . In each column the value of ΔE is with respect to corresponding magnetic structure 1. One can find that the MnBi_2Te_4 layer favors FM coupling with CrI_3 and AFM coupling to its neighboring MnBi_2Te_4 .

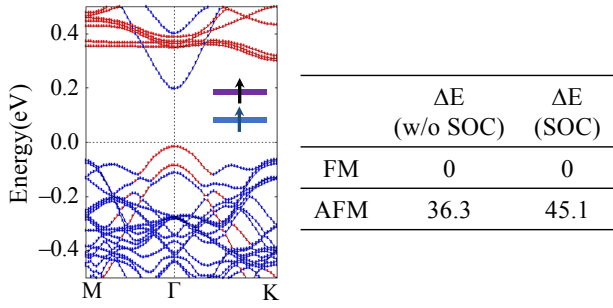


FIG. S3. The total energy ΔE for different magnetic coupling of the interface for 1-SL 3×3 MnBi_2Te_4 on 2×2 CrI_3 . Here the magnetic coupling energy is still in the order of 40 meV and FM is favored in energy. For the FM coupling, the band structure exhibits an energy gap as a magnetic insulator. The red curves are $\text{Cr-}e_g$ bands and blue curves are MnBi_2Te_4 states.

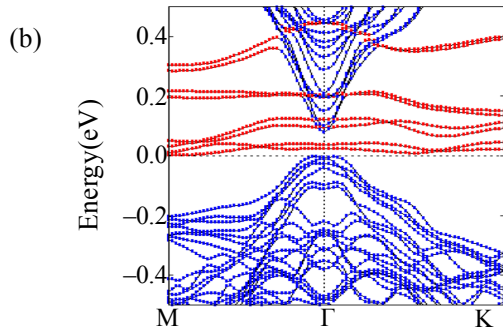
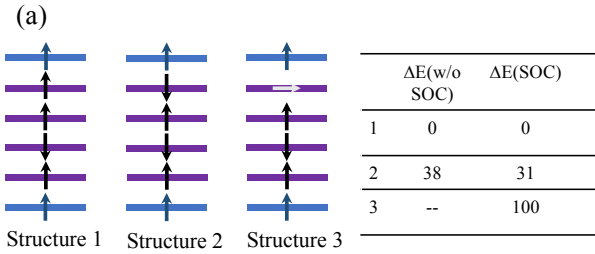


FIG. S4. (a) Different magnetic structures for 4-SL-thick MnBi_2Te_4 sandwiched between two CrI_3 layers and their total energies with respect to structure 1. We have tested different magnetic structures including the in-plane moment. The top MnBi_2Te_4 SL is switched to align parallel to the upper CrI_3 in spins, because of the exchange bias effect. (b) The band structure of structure 1. The red curves are $\text{Cr-}e_g$ bands and blue curves are MnBi_2Te_4 states.

3L ($\sqrt{3}\times\sqrt{3}$) MnBi₂Te₄ on (1×1) CrI₃

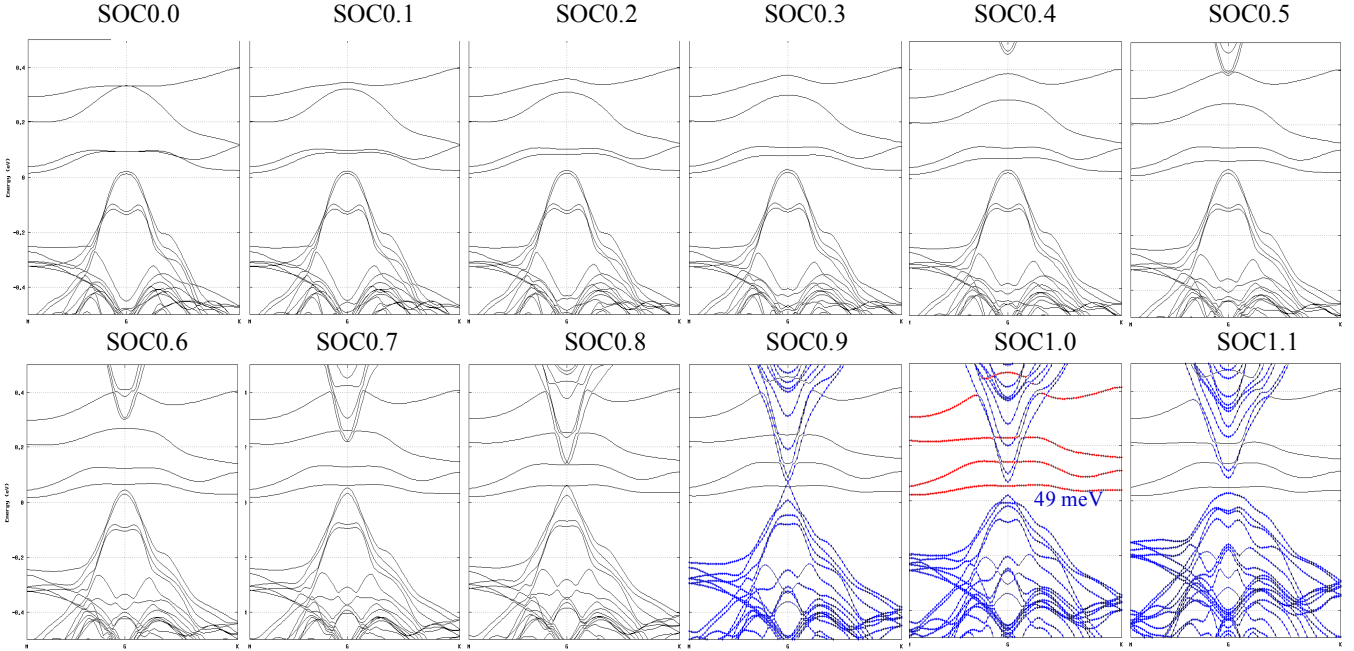


FIG. S5. Band structure evolution for 3-SL-thick MnBi₂Te₄ /CrI₃ heterostructure with varying SOC strength from 0 to 110%. There is a gap-closing near SOC =90%, indicating a topological phase transition from a trivial magnetic insulator to a QAH insulator.

5L ($\sqrt{3}\times\sqrt{3}$) MnBi₂Te₄ on (1×1) CrI₃

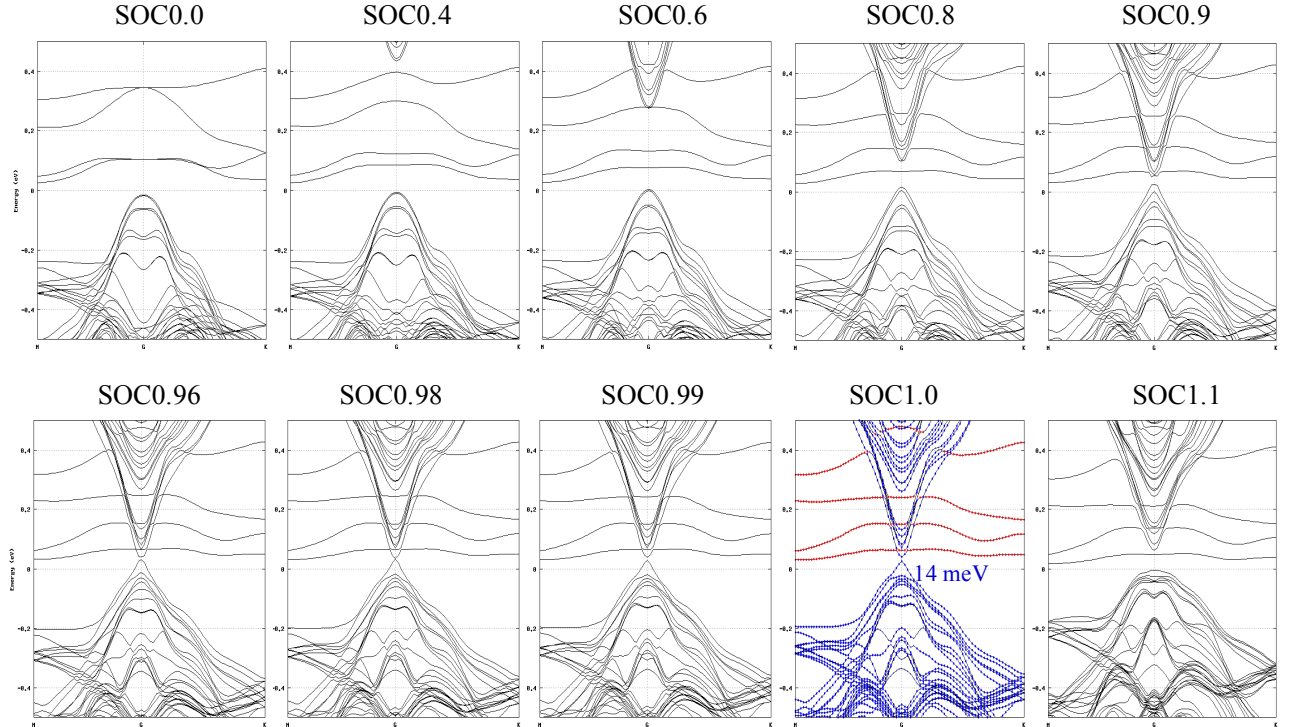


FIG. S6. Band structure evolution for 5-SL-thick MnBi₂Te₄ /CrI₃ heterostructure with varying SOC strength from 0 to 110%. There is a gap-closing near SOC =98%, indicating a topological phase transition from a trivial magnetic insulator to a QAH insulator.